CIRP Journal of Manufacturing Science and Technology 41 (2023) 365–379

Contents lists available at ScienceDirect

CIRP Journal of Manufacturing Science and Technology

journal homepage: www.elsevier.com/locate/cirpj

Characterization of microstructure and residual stress following the friction stir welding of dissimilar aluminum alloys

Nicholas Sabry *, Joshua Stroh, Dimitry Sediako

High-Performance Powertrain Materials Laboratory, University of British Columbia, 1137 Alumni Ave, Kelowna, BC V1V 1V7, Canada

ARTICLE INFO

Available online xxxx

Keywords:
Friction Stir Welding (FSW)
Solid State Welding
Aluminum Alloy
Residual Stress
Neutron Diffraction
EBSD

ABSTRACT

Friction-stir-welding (FSW) has gained importance as an effective way to join dissimilar materials due to its solid-state nature. However, FSW produces substantial residual stresses in aluminum welding, often deteriorating the component's structural performance and reliability. In the current study, the *d*-spacing (inter-atomic distance) of several locations on a battery tray and stress-free reference samples are measured with neutron diffraction to calculate the residual stresses in a lap 6061 to A365 dissimilar friction-stir-weld. Furthermore, the present study connects the measured residual stress to microstructure properties through electron backscatter diffraction (EBSD) and optical microscopy analyses. The EBSD results indicate that the FSW operation affects the grains' orientation, thereby producing location-specific directionally varying elasticity across the weldment. This varied elasticity creates unique *d*-spacing profiles even in the stress-free material. Additionally, the resulting stressed and stress-free *d*-spacing profiles show dependencies on the FSW tool geometry, traverse direction, and rotational direction. Lastly, this study suggests that the final component residual stress can be influenced by the sequence of multi-pass welds contributing to a rise in temperature in the presence of a completed weld relaxing its residual stress.

Introduction

Joining cast aluminum (Al) components with wrought metals is becoming an efficient design strategy frequently utilized in the automotive industry. For example, this strategy has recently been employed to further develop complex and large body structures that require lightweight solutions by enabling different manufacturing techniques such as casting, extrusion and forming in a single joint component. One such casting technique is high-pressure die-casting (HPDC), which utilizes pressure-injected molten aluminum into a steel mold to form thin-walled components. After the system's initial cost, the HPDC technique is fast and inexpensive in producing components as it delivers near-net structures with minimal post-cast machining required [21]. However, during the HPDC operation, turbulence is generated in the liquid metal due to the high velocity required to produce thin-walled castings. Unfortunately, turbulent conditions cause porosity and gas entrapment. As a result, the entrapped gas of air, hydrogen and vaporized die lubricants render fusion welding an impractical joining method unless expensive vacuum HPDC equipment is employed to minimize porosity [41]. Furthermore, fusion welding struggles with dissimilar-material welding as fusion requires the materials to melt before joining. Because dissimilar materials have different melting temperatures, the alloying elements required for strength and other properties burn in the material with lower melting temperatures before the second material reaches the required temperature for fusion, creating a compromised weld [39]. Additionally, there are several other challenges related to dissimilar welding due to differences in the joined materials' mechanical, physical, chemical, and metallurgical properties [22,14,6]. While there are still obstacles to surmount, the FSW technique invented by Wayne Thomas at TWI Ltd in 1991 [42] has successfully been demonstrated to join dissimilar materials in a solid-state, i.e., below-melting temperature [5,18,19,19,4]. The solid-state nature of FSW avoids many problems, one of which is the joining of materials with different melting temperatures. The joining of dissimilar materials with FSW is achieved by severe plastic deformation of both materials, utilizing heat generated by a rotating tool plunged into the workpiece and advanced along the weld joint, mechanically mixing and forging plasticized dissimilar material

Abbreviations: FSW, Friction-Stir-Welding; HPDC, High-Pressure Die Casting; SEM, Scanning Electron Microscope; EDS, Energy-Dispersive X-Ray Spectroscopy; EBSD, Electron backscatter diffraction; IPF, Inverse Pole Figure; GROD, Grain Relative Orientation Deviation; Al, Aluminum; Si, Silicon; DXZ, Dynamically Recrystallized Zone; TMAZ, Thermo-Mechanically Affected Zone; HAZ, Heat-Affected Zone

* Corresponding author.
E-mail addresses: nsabry@mail.ubc.ca (N. Sabry), joshua.stroh@ubc.ca (J. Stroh), Dimitry.Sediako@ubc.ca (D. Sediako).

https://doi.org/10.1016/j.cirpj.2022.11.021
1755-5817/

together [8]. The severe plastic deformation leads to dynamic grain recrystallization, enabling the flow of plasticized material occurring in the solid-state weld [44]. Consequently, the recrystallization results in the formation of equiaxed and submicron grains in the weld zone after complete solidification. Therefore, FSW is a highly effective method for joining dissimilar materials, as the operation produces a weld joint with high mechanical strength due to the associated reduction of grains and the operation's solid-state nature [28].

Although the FSW method is effective in joining dissimilar materials, the heat generated during the operation and subsequent cooling of the body leads to the evolution of residual stress in that body. Typically for similar-alloy aluminum friction-stir-welds (FSWs), the maximum tensile residual stresses are on either side of the weld line, with lower residual stresses in between, forming an "M" shaped stress profile distribution as shown in Richards et al. [35]. However, this stress profile is heavily influenced by several factors, including the heat generation of the tool geometry shown in Giorgi et al. [11]. The effect of tool rotational speed is shown by He et al. [13]. The effect of tool traverse speed is shown in Peel et al. [34]. Finally, the effect of plunging force is shown by Nile et al. [29]. Giorgi et al. [11] show an example specific to tool geometry. They analyzed the effect of the shoulder geometry on the residual stress profile on a 1.5 mm thick 6082-T6 aluminum sheet. It was observed that when the tool geometry was modified, the tool's heat generation in the material was influenced significantly. As a result, it was concluded that tool geometries with a larger contact area between the tool shoulder and material surface produced higher peak temperatures, decreasing the maximum tensile residual stress [11]. In comparison, Aval [3] examined the effect of rotational speed and traverse speed on the resulting residual stress in 8 mm thick dissimilar welded 6082-T6 and 7075-T6 aluminum plates. They found that as the rotational speed increased and the traverse speed decreased, both actions increased the material's heat generation, raised peak temperatures, and decreased the maximum tensile residual stress. The result of additional heat input and its effects on residual stress for Aval [3] contradicts the result of Giorgi et al. [11]. The contradicting results might be explained by Richards et al. [36], who described that the stress profile from FSW is due to the misfit of plastic strains that are introduced through steep temperature gradients as heat is generated from the FSW operation and distributed into the component during the advancement of the tool during welding. Therefore, combining the conclusions presented in the available literature suggests that peak temperatures alone do not determine the maximum tensile residual stress. Instead, the gradient in temperature or, more specifically, the material cooling rate and its uniformity has a more pronounced influence on the maximum tensile residual stress. The above statement is supported by the results from Campanelli et al. [7], who analyzed the effects of preheating the weld zone with a high-powered laser. They found that by preheating the work material, the peak temperatures increased, and the maximum tensile stress decreased, not because of the increased peak temperature but due to a control of the cooling rate, which reduced the steep gradients in temperature that the material experienced during welding. Additionally, there might be a significant difference in the cooling rate between FSW operations conducted on similar welded material and dissimilar welded material. Where FSW is conducted on dissimilar material, one must also consider the weld joint's abrupt property changes due to the weldment's heterogeneity. If, for example, thermal expansion coefficients of dissimilar metals vary significantly, it will give rise to the internal stress evolution in the weldment during every temperature change [23]. Whether the FSW operation is conducted on dissimilar or similar material, a significant amount of residual stress develops from the inevitable temperature gradients generated during the operation. Depending on the amount and type of residual stress, the friction-stir-welded component's structural performance, reliability, and service life may be reduced considerably.

A few mechanisms that heavily depend on the type and amount of residual stress in a component are fatigue crack propagation and distortion. For example, cracking caused by fatigue will self-arrest in compressive residual stress fields and propagate in tensile residual stress fields [43]. Additionally, if the amount of residual stress surpasses the yield stress of the base material, the component can distort in response not only due to tensile stress surpassing yield stress but by the entire magnitude of the difference between the peak tension and peak compression. The distortion mechanism is particularly pronounced in thin-walled HPDC structures (i.e., reduced cross-sectional areas) [25]. Therefore, a comprehensive understanding of the residual stress is required to maintain the longevity of consistent and high-quality friction-stir welds on HPDC components required in the automotive industry.

The present study focuses on joining a thin-walled HPDC component (A365) to several plates (6061) utilizing FSW. The joined component completes the manufacturing stage of an electric vehicle battery tray; however, the welding operation distorts the component due to the generation of residual stress. In order to investigate the residual stress that leads to the distortion of the component, this study utilizes neutron diffraction for its deep non-destructive material penetration, allowing for the residual stress measurement in an unaltered battery tray. Furthermore, the residual stress profile is linked to microstructure marks left by the FSW operation, utilizing an optical microscope and EBSD. This evaluation enables a better understanding and application of many parameters, such as tool geometry, weld direction, and initial temperature conditions, to minimize high stress evolution in FSW components.

Experimental details

Materials and weld process

In this study, several 6061-T6 aluminum plates with a 2 mm thickness are friction stir welded to a A365 high-pressure die-casted aluminum battery tray with varying thicknesses. The plate and casting are joined in a lap weld configuration (see Fig. 1b). The tool is plunged through the entirety of the 2 mm plate and slightly into the A365 casting to provide a solid bond between the two materials.

Table 1 lists the chemical composition of the 6061 and A365 alloys. The difference in chemical composition and processing leads to different precipitates or particles that locally change the stiffness and other properties of aluminum alloys (see Table 1).

A significant difference between A365 (cast) and 6061 (wrought) alloys is in the silicon composition, as one benefit of additional silicon is the increase in cast fluidity of the A365 alloy when the molten material is forced throughout the die in the HPDC operation [40]. However, with the increase in silicon, there is a corresponding decrease in the thermal expansion coefficient, which could have significant implications as the materials are heated and cooled through welding [15]. The HPDC operation and subsequent FSW used to manufacture the battery tray was conducted at the Nemak Alabama plant, United States. The manufacturing begins by casting the battery tray's main structure and coolant channels with the A365 aluminum alloy. Because the HPDC process is limited in creating internal geometries, the FSW operation is required to seal all exposed cooling channels with 6061 plates (see Fig. 1a). Unfortunately, the FSW operation leaves behind a “keyhole” defect where the tool is retracted at the end of the operation (see Fig. 3). This portion of the weld is the weakest, and several methods exist to repair this defect [26]. However, the keyhole defect falls outside the scope of the present study. Nonetheless, the FSW operation in this study utilizes a tool with a 12 mm diameter shoulder that is filleted to a 14 mm diameter with a triangular M12 threaded 2.2 mm long pin (see

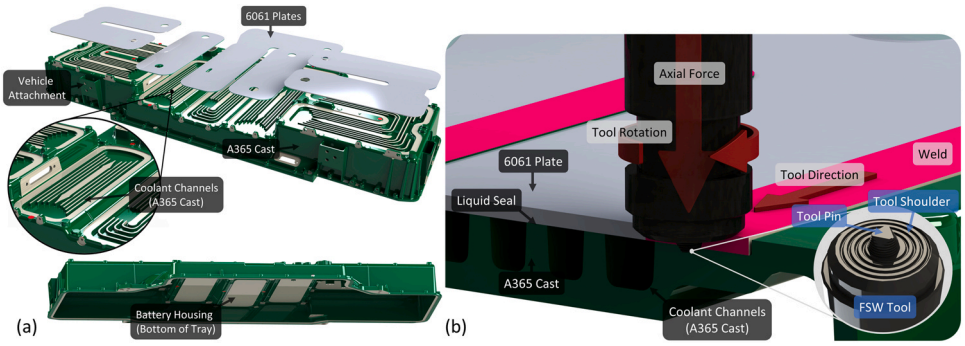

Fig. 1. (a) Battery tray coolant channels, cast structure, and plate position (b) Cross-section of battery tray coolant channel with weld path in magenta.

Table 1
6061 and A365 chemical composition (shown in wt%).

	Si	Mg	Cu	Fe	Zn	Mn	Cr	Ti	Ni	Sr	Al
6061	0.70	0.90	0.30	0.60	0.20	0.05	0.3	0.10	0.05	**	Bal.
A365	9.73	0.17	0.004	0.11	**	0.560	**	0.07	**	0.02	Bal.

Fig. 1b). The operation is divided between peripheral and non-peripheral welds (see Fig. 2), with different traverse speeds, rotational speeds, and plunging forces, as described in Table 2.

Please note that an NDA protects the values in Table 2; regardless, the magnitude values are irrelevant to this study's purpose. Instead, the relative magnitudes are the critical consideration when comparing each weld group.

Microstructure sample preparation

The microstructural analysis is completed on a metallurgical sample extracted from the cross-section of a weld line that combines the 6061-wrought and A365-cast material (see Fig. 3). First, the sample was mounted and polished following the principles outlined in the ASTM E3–11 standard. Following polishing, the specimen was electro-etched using Barker's etchant (5 ml of fluoroboric acid diluted with 200 ml of distilled water) for 15 s with an applied voltage of 30 V through a stainless-steel anode and cathode. Following etching, the sample was rinsed in distilled water and air-dried. Next, a microstructure analysis was completed with an optical microscope and scanning electron microscope (SEM) utilizing acquisition and processing software for composition analysis.

Additionally, electron backscatter diffraction (EBSD) was used for grain orientation characterization. The EBSD procedure requires separate samples due to the extra precision necessary for reasonable grain detection rates. The EBSD sample followed the same polishing procedure as the SEM samples. However, following the last polish stage, a vibrating polisher with colloidal silica blue (10 pHs) as the suspension was used, requiring 4–5 h to reduce scratch sizes to 0.06 µm.

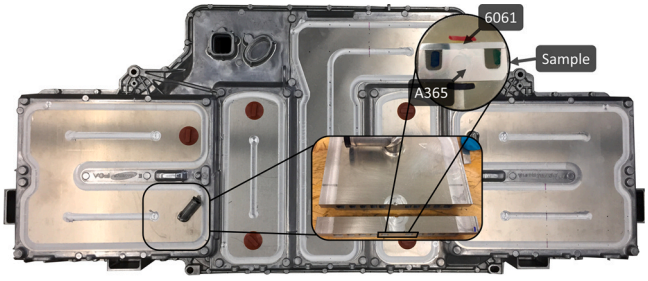

Fig. 3. Location of metallurgical sample.

Neutron diffraction and tensile testing

Neutron diffraction experiments were conducted in the High Flux Isotope Reactor facility at Oak Ridge National Laboratory on the HB-2B High-Intensity Diffractometer for Residual stress Analysis

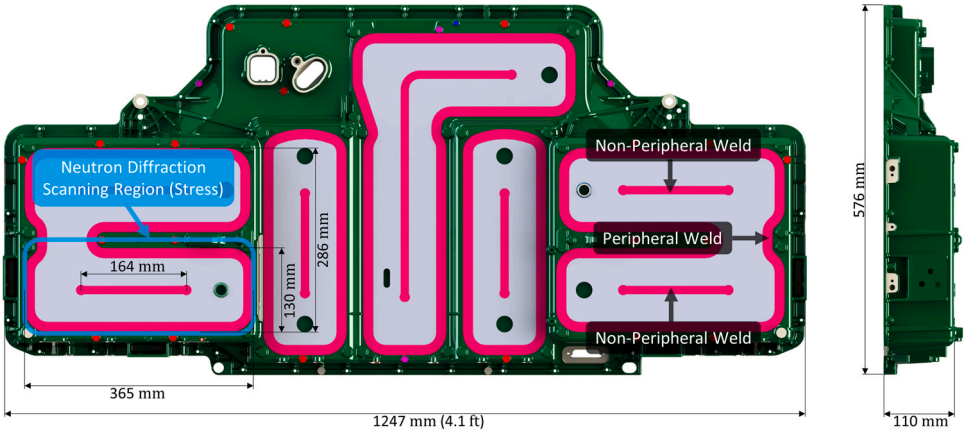

Fig. 2. Peripheral and non-peripheral weld placement on the battery tray, welds in magenta and scanning region outlined in blue.

Table 2
FSW processing conditions.

Weld Type	Plunge Depth (mm)	Dwell Time (s)	Traverse Speed (mm/min)	Rotational Speed (rpm)	Plunge Force (kN)	Plunge Feed (mm/min)	Withdraw Feed (mm/min)
Peripheral	A	B * 6	C	D	E	F	G
Non-peripheral	A	B	C * 2	D* 2	E * 2	F	G

(HIDRA) instrument. The specific methods utilized in the present study to acquire strain were applied by Sediako et al. [37], employing the equations established by Hutchings et al. [17] to determine the stress in all three orientations (longitudinal-X, transverse-Y, and normal-Z) on the aluminum battery tray. Furthermore, the breakthrough work by Holden and Schajer [16] formulated in detail the method of experimental elastic strains and stresses in terms of lattice interplanar spacing measurements.

According to Bragg's law, the {311} atomic planes of the aluminum battery tray diffract the incident monochromatic neutron beam of wavelength $\lambda = 1.7232$ Å to create a diffraction pattern where a peak at an angle of θ_{hkl} can be found. This angle (θ_{hkl}) is in the vicinity of 88–89° depending on the strain experienced by the atomic planes for the {311} atomic planes diffracted at a wavelength $\lambda = 1.7232$ Å. The diffracted planes create a nearly square gauge volume (2 mm in width, 2 mm in depth and 8 mm in height) in the sample material for this study. In addition to the nearly square shape gauge volume produced by the {311} atomic planes, ISO standard 2143 outlines that these planes are not affected by intergranular stress in the material; therefore, only macro scale stress from the manufacturing process is detected. After pattern collection, Bragg's law relates the θ_{hkl} obtained from the diffraction pattern and the wavelength λ to the position of each d_{hkl} plane, otherwise known as d-spacing, which is the distance between parallel planes of atoms in the gauge volume. Bragg's Law (Eq. 1) incorporates the following symbols: n for the atomic order, λ for the wavelength, d_{hkl} for the d-spacing, and θ_{hkl} for the diffraction angle.

$$n\lambda = 2d_{hkl}\sin(\theta_{hkl}) \tag{1}$$

In this study, neutron diffraction is utilized to obtain the d-spacing in a specific component direction. The measured component direction is identified by the scattering vector (Q), which is the subtraction of the diffracted vector (K_f) and the incident vector (K_i). The scattering vector is perpendicular to the measured plane (see Fig. 6). The sample can then be rotated by 90 degrees to obtain the strain value measured in the next direction for the same location. From the d-spacing measurements, strain can be calculated with Eq. 2. As shown in Eq. 2, stress-free (d_0) reference is required as a baseline to quantify the strain (ε) in the stressed (d) material.

$$\varepsilon = \frac{d - d_0}{d_0} \tag{2}$$

Consequently, two individual diffraction scans are required (i.e., for a stressed and a stress-free material). With both angular positions of the peak acquired, the d-spacing of the stressed (d) and stress-free (d_0) material is determined, utilizing Eq. 1. Then Eq. 2 is utilized to find the strain experienced by the material. Measuring the position of the diffracted peaks for the stressed (d) and stress-free (d_0) material and determining the difference in the peak position to calculate strain (ε) is known as the peak shift method. The above-described process is complete for strain in three orientations (longitudinal-X, transverse-Y, and normal-Z), allowing the calculation of stress in each orientation with Eq. 3 [31]. Where σ_{xyz} is the stress for each orthogonal direction in MPa, E is the modulus of elasticity in GPa, v is Poisson's ratio, and ε_{xyz} is the strain for each direction.

$$\sigma_{x,y,z} = \left(\frac{E}{(1+v)}\right)\left[\varepsilon_{x,y,z} + \frac{v}{1-2v}(\varepsilon_x + \varepsilon_y + \varepsilon_z)\right] \tag{3}$$

Fig. 4a indicates the location of an example scan line in the middle of the battery tray as an overview of the procedure of the peak shift method. The following image includes the diffraction pattern of each scan point along the example scan line (see Fig. 4b). First, the diffraction patterns must be fitted to obtain the peak center angle (see Fig. 4c). The fitting is done with a pseudo-Voigt function as the line

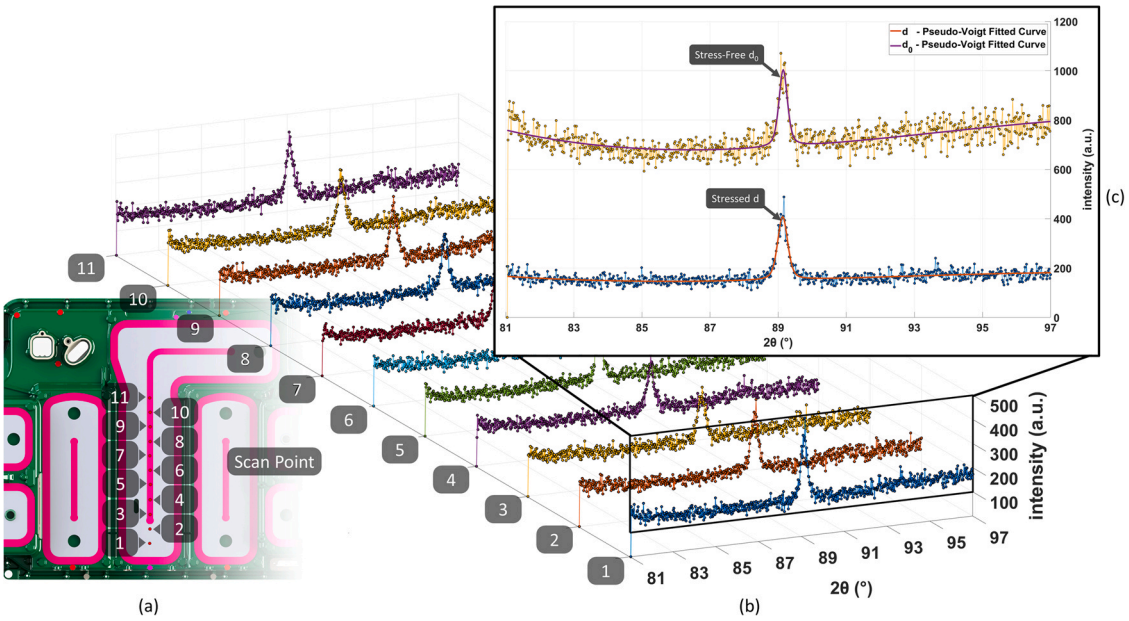

Fig. 4. (a) Scan point locations (b) Diffraction pattern of each scan point (c) Pseudo-Voigt fitted curve for point one and the stress-free reference pattern.

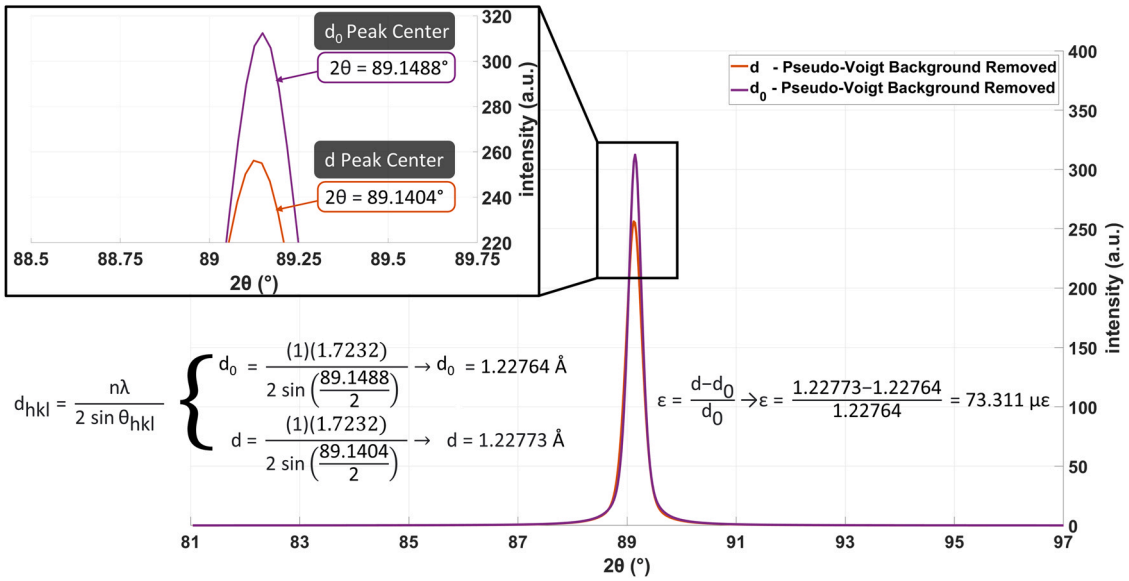

Fig. 5. Calculating strain from shifted diffraction peaks with background removed.

profile for the diffraction patterns. The pseudo-Voigt function is a linear combination of the Gauss and Lorentz functions and is the most common line-fitting function for neutron diffraction data [33]. As mentioned above, a stress-free reference is required to find strain by utilizing the shifting peaks between the stress-free and stressed patterns. Fig. 4c contains the aforementioned diffraction patterns, with the stress-free pattern situated above the stressed pattern. The stress-free reference is situated above the stressed pattern because it has a different background intensity. Therefore, the backgrounds are removed to visually compare the shifting peaks, as shown in Fig. 5. With the pseudo-Voigt fitted peaks, each peak center angle can be obtained and converted into the distance between parallel planes of atoms (d-spacing) utilizing Braggs law (Eq. 1), given that θ_{hkl} is half of 2θ. Following Bragg's calculation, the d-spacing is converted to strain with Eq. 2, shown in Fig. 5. Since the stressed peak is shifted to the left of the stress-free peak, the resulting strain is tensile, as shown at the end of the calculation in Fig. 5. For comparison, the resulting strain would have been compressive if the stressed peak had shifted to the right of the stress-free peak.

In the present study, the scanning is complete across several welds. Because the welding action changes the grain structure, size, orientation and chemical composition, stress-free material is required for many locations to account for the differences in the material across several welds. Therefore, a comb-style set of d_0 stress-free samples were extracted from an identical battery tray (see Fig. 6). The stress-free reference is obtained by cutting the material

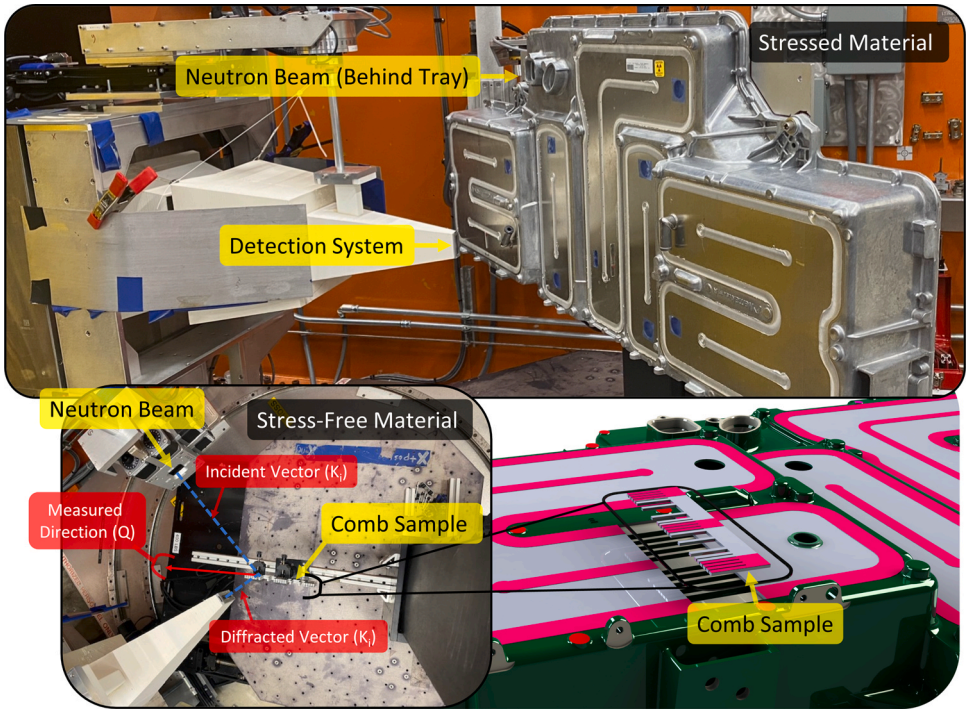

Fig. 6. Stressed sample and stress-free comb sample in HIDRA instrument.

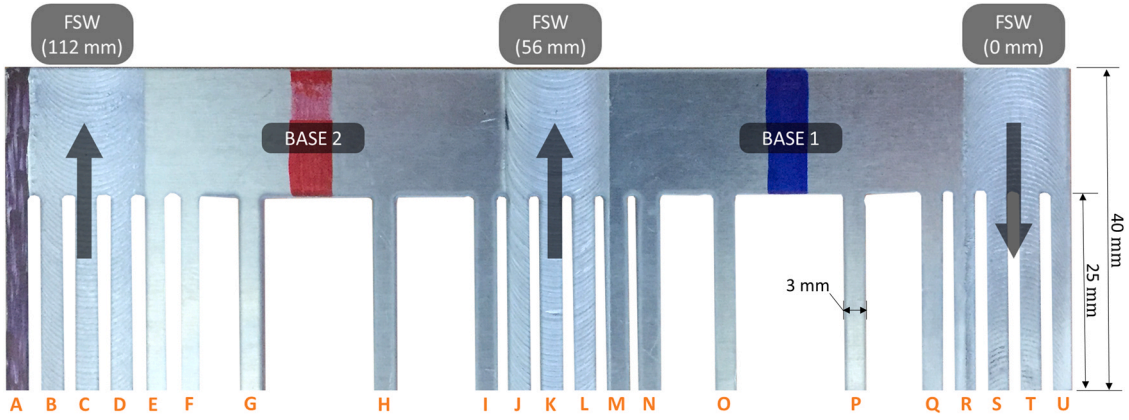

Fig. 7. Stress-free comb sample and the direction of the tool during welding shown with the black arrows.

into small sections alleviating stress from the surrounding material. The comb-sample accounts for the compositional and microstructural differences across the weld caused by the thermo-mechanical cycle of welding, as local fluctuations cause changes in the stress-free lattice. Each tooth of the comb takes those fluctuations into account while having an insufficient dimension to hold a macro-stress field in the scanning direction. Therefore, the teeth dimension (see Fig. 7) on the comb was chosen as all macro stress of type 1 is alleviated in any direction perpendicular to the long direction of the tooth [17].

However, stress-free measurements are often obtained from small cubes machined from the weld instead of a comb-style sample. Ganguly et al. [10] compared both measurement methods and found that the teeth size is small enough to alleviate the macro-stress field except for the direction of maximum dimension. Furthermore, a comparative study by Paradowska et al. [32] between the comb and cube methods measured a near-exact *d*-spacing value for the stress-free references. Hence, the comb sample has previously been utilized as a stress-free reference in Sediako et al. [37] and Liu et al. [24]. Consequently, in the present study, the stressed material is measured directly from the original un-cut battery tray, and the stress-free material is measured from the comb stress-free samples, shown in Fig. 6.

Results and discussion

Lattice spacing, strain, and EBSD

The scanning was conducted in a $400 \times 400\ mm^2$ area at the bottom left of the battery tray (see Fig. 2), where the HIDRA instrument could be orientated to obtain all three directions of strain required for stress analysis. As the scanning occurred over several FSWs, stress-free samples were required that encompassed each weld. The stress-free comb sample used is shown in Fig. 8, which

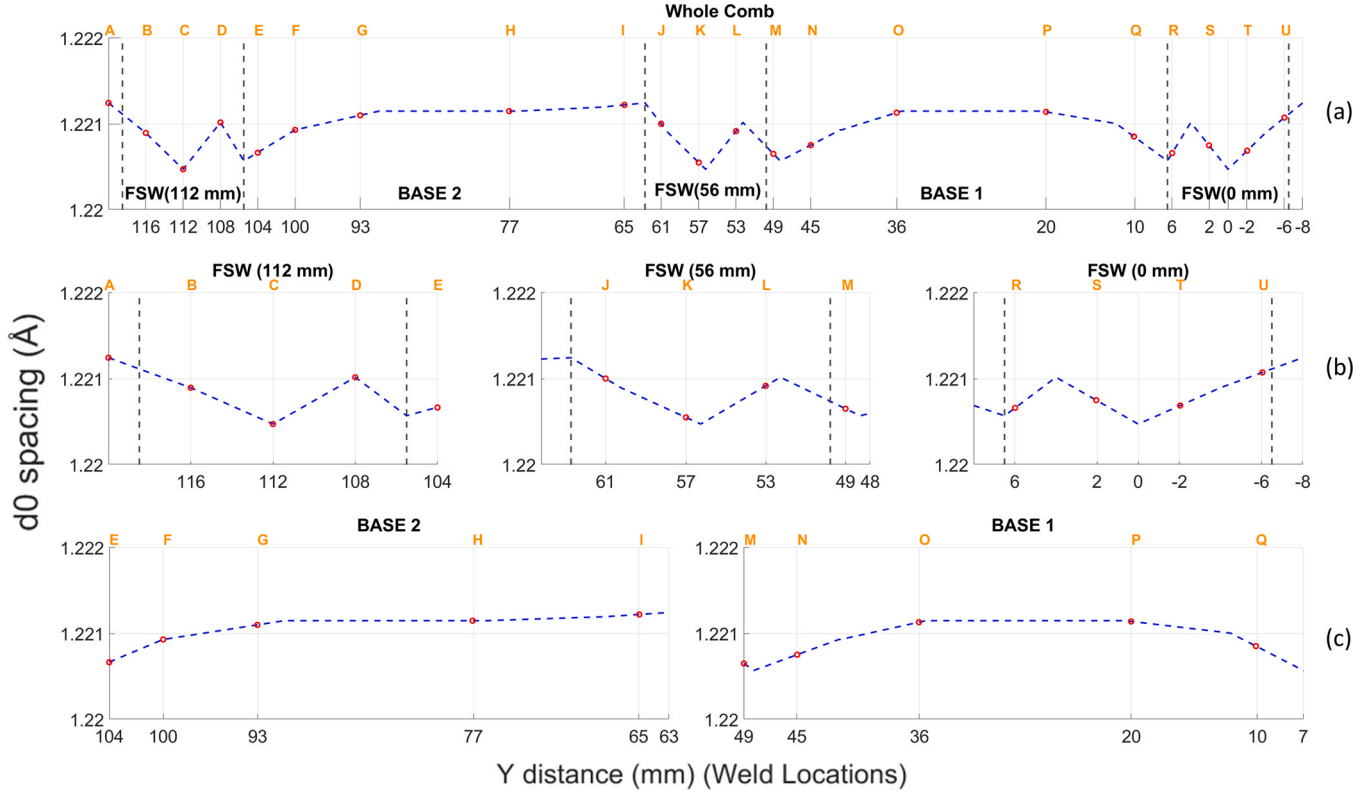

Fig. 8. (a) Stress-free comb sample data (b) Isolated welds (c) Isolated base.

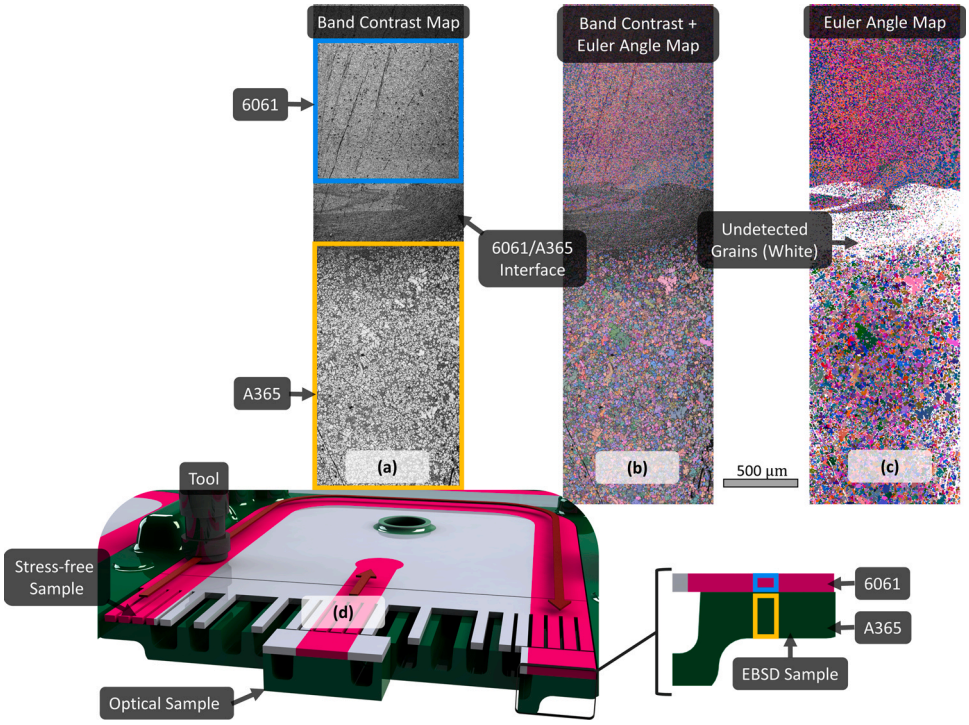

Fig. 9. (a) Band contrast map (b) Band contrast map and Euler angle map (c) Euler angle map.

contains the measured *d*-spacing profile for the comb stress-free sample, where a notable change in the d_0 value across the sample is seen, corresponding to the physical operations during welding. For example, in Fig. 8c, the stress-free *d*-spacing profile of the 56 and 112 mm weld is similar, and in both welds, the FSW tool is rotating and traversing in the same direction (see black arrows). However, at the 0 mm weld, the profile is a vertical mirror of the 56 and 112 mm profiles, corresponding to a change in tool rotation and direction. The changing d_0 value across the comb stress-free sample is due to the welding action changing the grain structure, grain size, grain orientation and chemical composition across the weld (see Fig. 8). This varying d_0 parameter across the weld line was also observed by [34] stating that significant errors in inferred residual stress would occur if a single value of d_0 were used for a diffraction-based experiment. The varying grain structure, size, and orientation of the crystalline structure that contributes to the changing d_0 throughout the sample are influenced by the strain rate, heat input, cooling rate, and direction of movement for the plasticized material during the FSW operation. On a processing level, these factors are primarily controlled by the geometry, direction and speed of the rotating and traversing FSW tool. The grain structure, size, and orientation of crystallites in this study are determined with the utilization of EBSD on the sample shown in Fig. 9.

Analysis with EBSD is based on the band contrast map created from the beam's interactions with the crystal structure (see Fig. 9a). These interactions create Kikuchi patterns that are detectable through EBSD [30]. Recording the Kikuchi lines and plotting their band contrast creates a map representing the contrast between grains and grain boundaries. No indexing or prior information on the crystal structure is required since the system is recording the intensity of the Kikuchi lines at each point, and an image can be constructed directly from the contrast of each set of lines. For example, in Fig. 9a, the grain boundaries produce less band contrast and appear dark on the map, while the grains produce more contrast and appear lighter on the map. Indexing structures allow for the addition of Euler angles into the maps (see Fig. 9b).

Euler angles define the difference in orientation between each crystal in the specimen and the globally defined axes (rolling direction, transverse direction, and normal direction). The crystal orientations and the global orientations do not match each other. The angle difference between the crystal and global axes is shown with Euler angles represented as red, blue, or green, where similar colors have comparable orientations (see Fig. 9b). Plotting the Euler map without the band contrast reveals all the grains the system could not index, as shown by the white areas on the map in Fig. 9c. Specifically, near the 6061-A365 interface, the recrystallized A365 grains are too small to identify for a 3-micron step size used in this scan. Similarly, throughout the A365 region, several white strips are not indexed, which is attributed to the Al-Si eutectic structure as this structure is much smaller than the scan step size. Nevertheless, with the intense variability in color, the Euler-colored maps are difficult to interpret and identify patterns as small orientation changes do not correspond to clear variations in the color scale. The Inverse Pole Figure (IPF) map overcomes the drawbacks in the Euler map by coloring specific crystal planes perpendicular to one of the chosen globally defined axes. The IPF map utilizes an aluminum cubic crystal's stereographic projection (3D to 2D mapping) to create a color key (see Fig. 10a). The color key retains only the [001], [101], and [111] directions from the aluminum crystal. Therefore, all crystals on the IPF map are colored by one of the crystal planes from the color key, depending on which crystal plane is perpendicular to the chosen global axis. For example, in Fig. 10e, a small portion of the overall map is viewed, where the global axis chosen is the normal direction, and the crystals are colored based on which plane is perpendicular to the normal direction.

However, if a different global axis is chosen, for example, the transverse direction, those same crystals would have a different plane perpendicular to the transverse direction resulting in a different color coating. Nevertheless, Fig. 10e is an ideal case and not all the crystals line up with one of the chosen directions and can be colored between one of the color key planes. Since the A365 material is cast with no post-processing, the crystals or grains are orientated

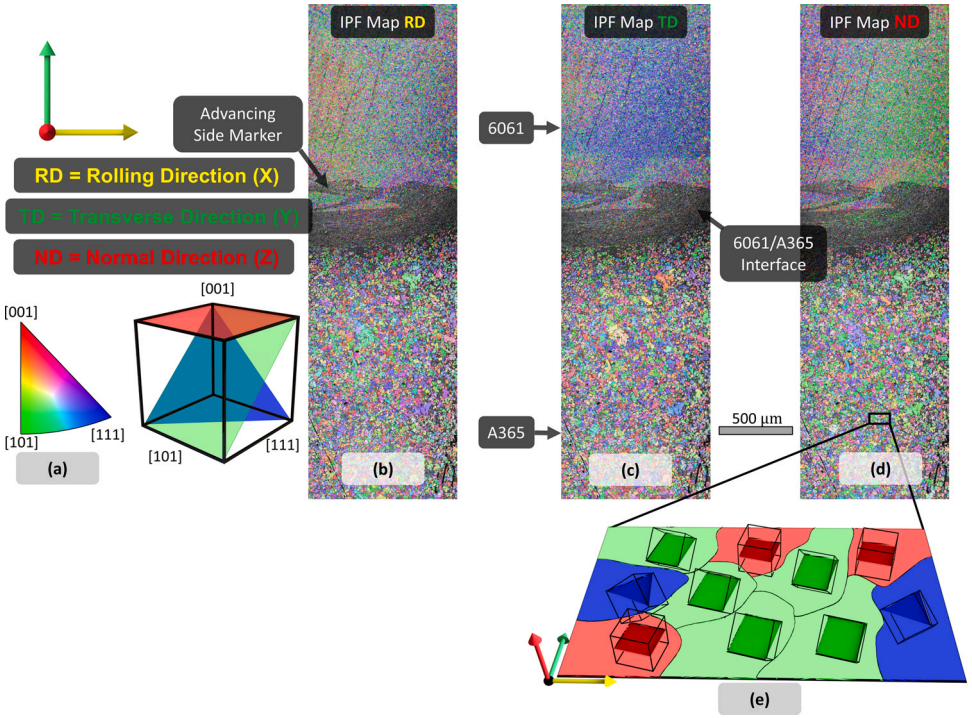

Fig. 10. (a) IPF color key (b) IPF map X-direction (c) IPF map Y-direction (d) IPF map Z-direction.

in no preferred direction, as shown with the yellow, orange, and pink grains that are in between the [001], [101], and [111] directions of the color key. However, for [111] crystal planes in the 6061 material, a large portion of these crystal planes are perpendicular to the transverse direction, as shown in Fig. 10c. The [101] crystal planes in the 6061 material are perpendicular to the normal direction, with a mixture of [001] and [111] planes perpendicular to the chosen direction on the left side of the map (see Fig. 10d). The [101] and [111] crystal planes ordering in the normal and transverse directions could be explained by the fact that the FSW tool advances down the weld line in these directions orientating the crystal planes accordingly. However, the ordering is not as evident in the rolling direction (Fig. 10b), which is the direction the FSW tool rotates. The [001] crystal plane is perpendicular to the rolling direction on the left (advancing side), then moving to the right; the crystal planes are colored yellow and then green, transitioning over from the [001] plane to the [101] plane. Finally, on the right, there is a mixture of [111], [101], and [001] crystal planes perpendicular to the rolling direction.

Residual stress

The stress measurements were obtained from the locations indicated in Fig. 11a for the left wing of the battery tray (the blue highlighted region in Fig. 2), where three orientations of stressed *d*-spacing could be measured. The scan on the left wing includes a line at − 81 mm, shown in blue, a red scan line at 0 mm, and a yellow scan line at 81 mm (see Fig. 11a and Fig. 11b). The gray dotted planes in Fig. 11b correspond to the weld location at 0, 56, and 112 mm from the component reference in Fig. 11a. The 3D stress profile is shown in Fig. 11b, and the corresponding projected 2D profile is shown in Fig. 11c. This data presentation method is utilized throughout the remainder of this paper. Moreover, this paper presents data for the longitudinal-X, transverse-Y, and normal-Z directions (see Fig. 11a

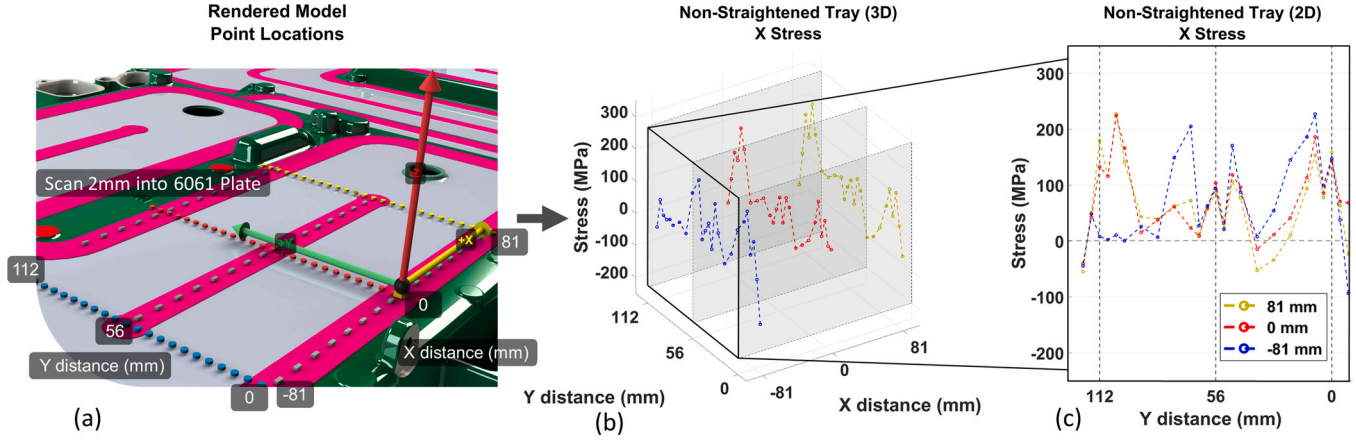

Fig. 11. (a) Visualization of scan point locations (b) Three-dimensional view of X-direction stress data (c) Two-dimensional view of X-direction stress data **(color required in print)**.

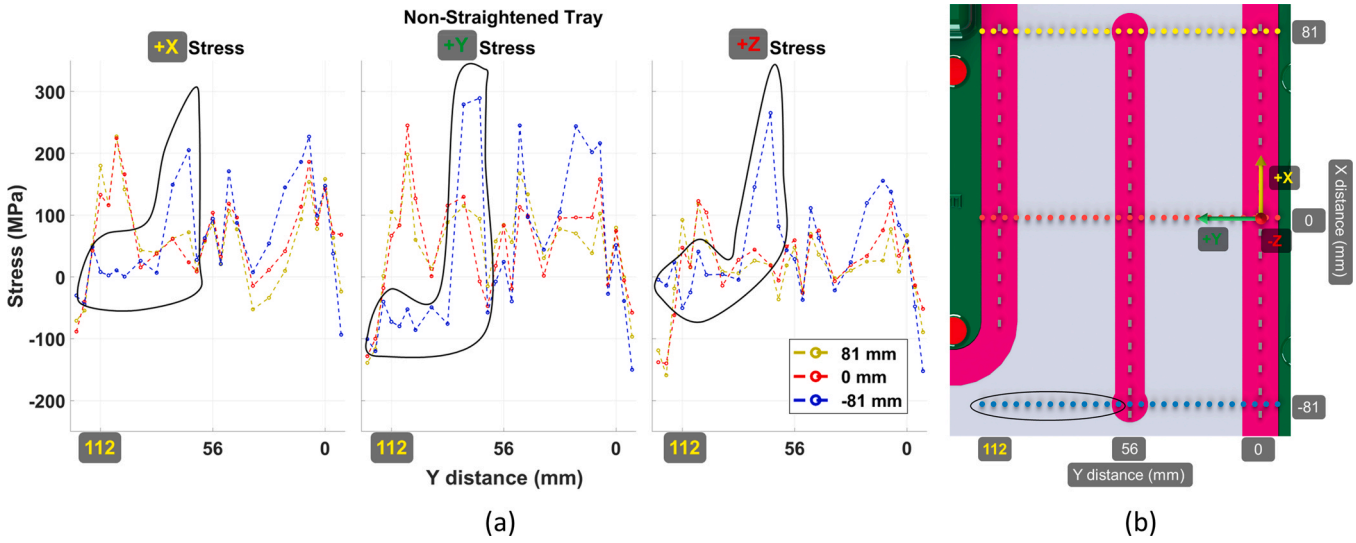

Fig. 12. (a) X, Y, and Z stress directions (b) Top view of scanned location highlighting the portion of the blue scan line that does not intersect a weld.

for the directions), corresponding to residual stress measured in the X-direction, Y-direction, and Z-direction. The stress measurements are spaced out a few millimeters from each other, crossing three friction-stir welds from 0 to 112 mm in the Y distance for the images in Fig. 11. This Y distance spacing corresponds to the arrangement of the stress-free sample so that for each location, the stress-free data can be applied. For example, the stress-free measurements are applied directly for the yellow and red lines, shown in Fig. 12b; as these lines traverse over the three welds at 0, 56, and 112 mm, the exact layout situation in the comb stress-free samples (see Fig. 9d). However, only the first two welds at 0 and 56 mm intersect the blue scan line, as there is no weld at the 112 mm mark for the blue-scan line (see the black circle in Fig. 12b). Therefore, un-welded 6061 stress-free *d*-spacing values are used in the outlined region shown in Fig. 12b. Because the blue line does not intersect the weld, the maximum measured tensile stress is not on the 112 mm location; instead, high tension is in the location outlined in black for Fig. 12a. In comparison, the red and yellow scan lines that intersect with welds measure maximum tensile stress directly adjacent to the weld lines and decreased tensile or compression stress outside the direct weld zone (see Fig. 13). In the case of FSW, after part of the body's temperature is raised to welding temperatures and then starts to cool, there are significant differences in the cooling rate throughout the body. The difference in cooling rates experienced by the surface and depth of the body results in local differences in thermal contraction.

The formation of the X-direction stresses can be explained by the results of [35] predicting the formation of longitudinal-X direction stress as follows: the approaching FSW tool heats the material, resulting in the expansion of hot material. However, the neighboring

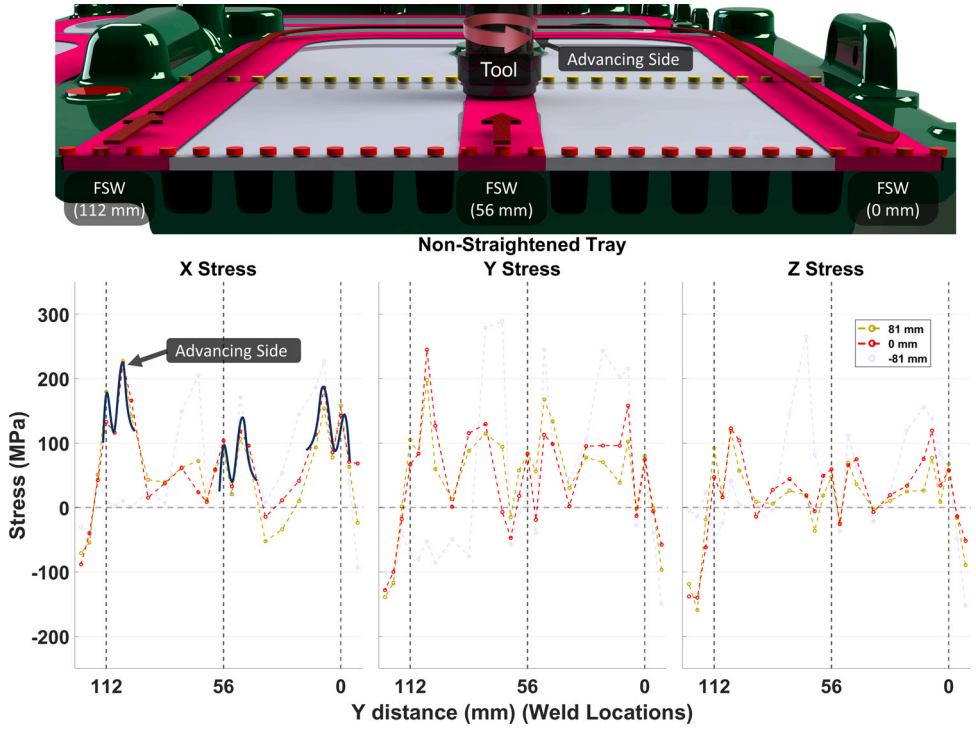

Fig. 13. Measured residual stress profile (red and yellow scan-lines).

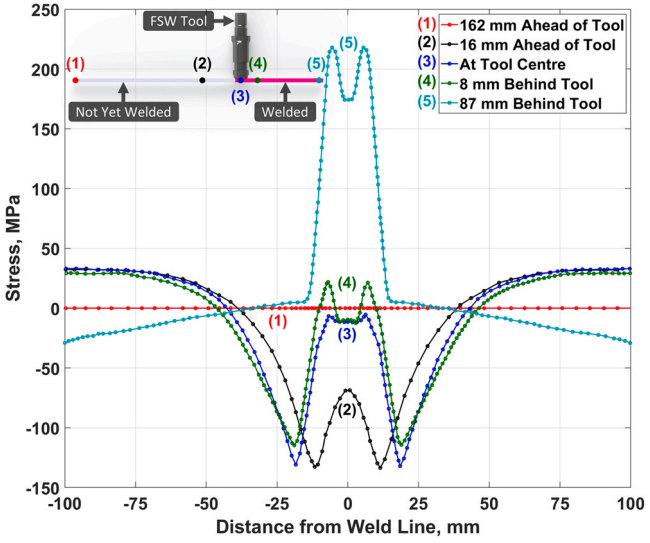

Fig. 14. Predicted longitudinal residual stress at different distances from the tool, adapted from the data presented in [35].

material between points 1 and 2 is colder; thus, the expanding hot material is constrained, generating compressive stress on the material (see Fig. 14-line 2).

This compressive stress will increase as the tool is approached from points 1–2 in Fig. 14 and, at some instant, exceed the local compressive yield strength leading to compressive plastic deformation. At this point, the material is very hot, not far below solidus temperatures; the yield strength at these temperatures is very low. Subsequently, the elastic component of stress is also low. Hence, there is a reduction in the measured compressive stress (see Fig. 14-line 3). As the tool continues its advance, the welded material behind the tool will cool down as the heat source (rotating tool) moves further away. The recently welded material at point 4 in Fig. 14 now cools and contracts; however, the neighboring material between points 4 and 5 is colder (see Fig. 14). Because the neighboring cold material restricts this contraction, tensile residual stress will start to generate (see Fig. 30-line 4). The tensile yield stress decreases rapidly with increasing temperature for high-strength aluminum alloys. Therefore, as the material directly behind the tool is at high temperatures, the local tensile yield stress will be low. Furthermore, the low yield stress limits the generation of residual stress as the magnitude of residual stress is determined by the material's elastic strain limit (before yielding) (see Fig. 30-line 4). Noting that as the temperature changes, the yield stress changes; the steep gradient in temperature directly outside the tool shoulder creates a differential in the amount of residual stress that can be generated due to the variation in local yield stress across that region (see Fig. 15).

Therefore, residual stress will develop more quickly at the lower temperature region outward of the tool shoulder, generating slightly higher residual stress at the edge of the weld zone. Subsequently, developing the characteristic 'M' shaped residual stress profile (Fig. 14-line 4). The yield stress will continue to increase as the tool traverses further from the material, reducing the temperature and allowing tensile residual stress to continue and generate (through an additional contraction) in the material's elasticity until the yield stress reaches its maximum at room-temperature (Fig. 14-line 5). Considering the differences between the simulated results of [35] and the measured residual stress in this study, it is important to note residual stress generated above the yield stress can result in plastic deformation of the material. Additionally, the plastic deformation below the recrystallization temperature can contribute to strain hardening. Therefore, a situation may arise where the weld conducted at double the rotational speed (56 mm weld), resulting in higher temperatures and strain rate, induces more plastic deformation into the material compared to the welds at slow rotational speed (0- and 112-mm weld). If significant strain-hardening effects were found in the 56 mm weld, that could support the idea of increased plastic deformation; however, this will be investigated in a future study.

Nevertheless, in all three weld cases, the residual stress builds up through thermal stress evolution during cooling. At this point, the uniformity and rate of cooling will determine how much thermal-generated residual stress is measured as yield stress increases with decreasing temperature. If the yield stress returns to a similar point and thermal contractions are comparable, then the residual stress is expected to be the same for each of the three peaks at 0, 56, and 112 mm welds, regardless of the process parameters. However, this is not the case, as seen by the 56 mm weld in Fig. 13, with substantially lower residual stress than the 0 and 112 mm welds; this may come down to the order of operations. For example, consider the sequence order of welding: first conducted is the 56 mm weld; after completion, the tool is retracted and plunged into the peripheral weld path line (see Fig. 2) that includes the 112 and 0 mm welds connected in a bend around the tray (see Fig. 13). The 56 mm weld has already started to cool, gaining back more yield strength and allowing residual stress formation with thermal contraction. Now that the tool is welding and generating heat at the peripheral bend path for the 0 and 112 mm welds, that heat conducts through the aluminum and relaxes the residual stress in the 56 mm weld. James [20] describes a weakly time-dependent temperature mechanism that causes the relaxation of the residual stresses; in the case of the aluminum battery tray cooling down to room temperature, this mechanism should be considered. The mechanism describes the relief of elastic strain through rapid thermal activation of dislocations in the presence of a temperature environment high enough to cause a sizeable reduction in the material yield strength. This mechanism necessitates that the yield strength approaches the value corresponding to the residual stress measured. The implication is that in the case of

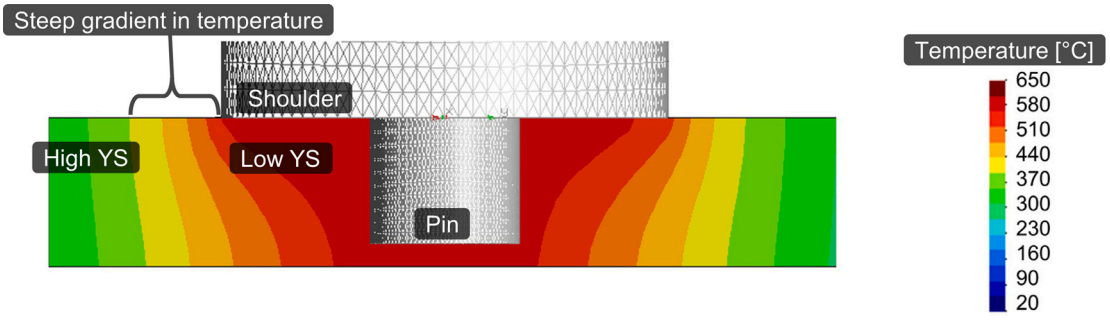

Fig. 15. FSW Temperature distribution map ("YS" – Yield Stress) adapted from [1].

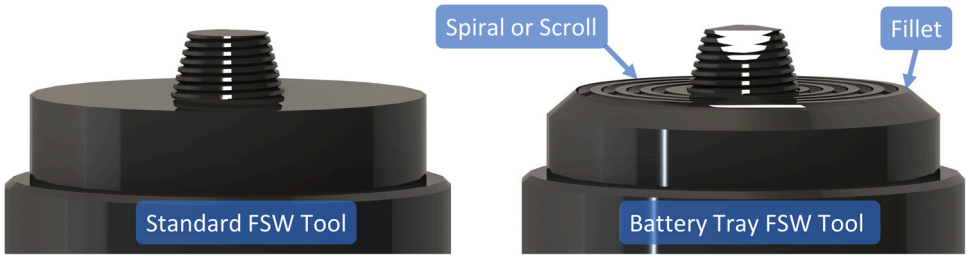

Fig. 16. Battery tray FSW tool compared to the typical FSW tool.

the FSWs, the peripheral welding generated enough heat to reduce the yield strength of the 56 mm weld to the measured residual stress state in Fig. 13 to allow the thermal activation of dislocations to occur and redistribute to that yield strength.

Another distinction that should be noted between the simulated profiles by [35] and the measured stress in the present study are the differences in the “M” shaped stress distribution; where the simulated profile did not consider how the “advancing” side of the tool generates more heat as compared to the “retreating side” of the tool. The impact leads to variance in heat input from the tool's advancing side, resulting in an asymmetric “M” shape with higher peak residual stresses on the advancing side (see Fig. 13). The advancing side marker follows the rotation of the tool resulting in a directionality dependence on residual stress formation. For example, the advancing side marker appears on the same side for the 56 and 112 mm welds with different stress magnitudes as the tool is rotating in the same direction (see Fig. 13), with low tensile magnitudes on the left, followed by a drop in stress, then maximum tensile magnitudes on the right. While at the 0 mm weld, the stress profile flips as the tool comes around the end of the battery tray to complete the bend in the peripheral weld path (see Fig. 13) and is now traversing out of the page, creating the advancing side marker on the left instead. The path and direction-dependent formation suggest that the residual stress profiles and resulting distortion may be controlled to some extent if the FSW tool's directionality is optimized. However, the tool's direction is not the only influence on the stress profile; tool geometry also heavily influences the asymmetric and offset "M" shape of the profile seen in Fig. 13. Typically the FSW process creates a centered "M" shaped residual stress profile that is characteristically found with the use of the standard flat shoulder and threaded circular pin FSW tools [35]. Analyzing this influence, Giorgi et al. [11] examined the effect of the shoulder geometry on the residual stress profile. They found that as the tool geometry was modified, the tool's heat generation and its input to the material were influenced significantly. As a result, the tool geometry impacts the residual stress profile with such a magnitude that either tension or compression can be observed [11]. Nevertheless, there are similarities between the profiles in Richards et al. [35] and the ones found in the present study, with the apparent difference being that the profiles in this study are not centered on the weld line. The off-centered profile is attributed to the differences between the tool geometry utilized to complete the welds in this study and the standard tool geometry that creates the centered "M" shaped residual stress profile (see Fig. 16). This suggests further that the resulting stress profile can be controlled not only with rotational and traversal speed but also with careful consideration of the tool's shape and geometry.

Microstructure

The grain refinement in the friction-stir-welded microstructure transpires during mechanical stirring in the dynamically recrystallized zone (DXZ). The tool pin causes intense plastic deformation in the depth of the material, which is pulled up to the tool shoulder from the retreating side of the weld and deposited on the advancing side, creating a unique marker signifying the advancing side shown in Fig. 17. Because the EBSD samples are taken from the 0 mm weld, the advancing side marker is on the left compared to the metallurgical sample taken from the 56 mm weld with an opposite tool direction and rotation, creating the marker on the right. In both

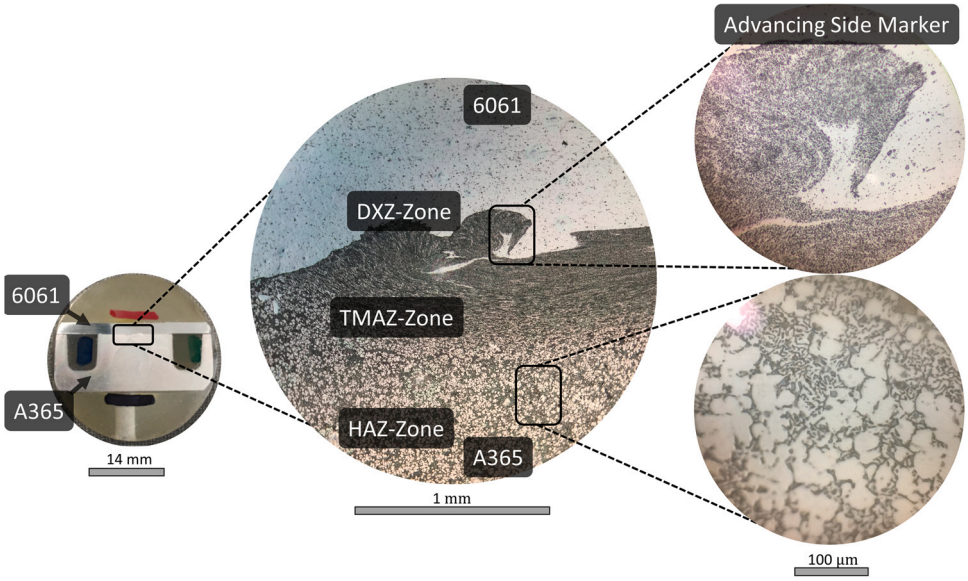

Fig. 17. Friction-stir-weld zones identified with an optical microscope.

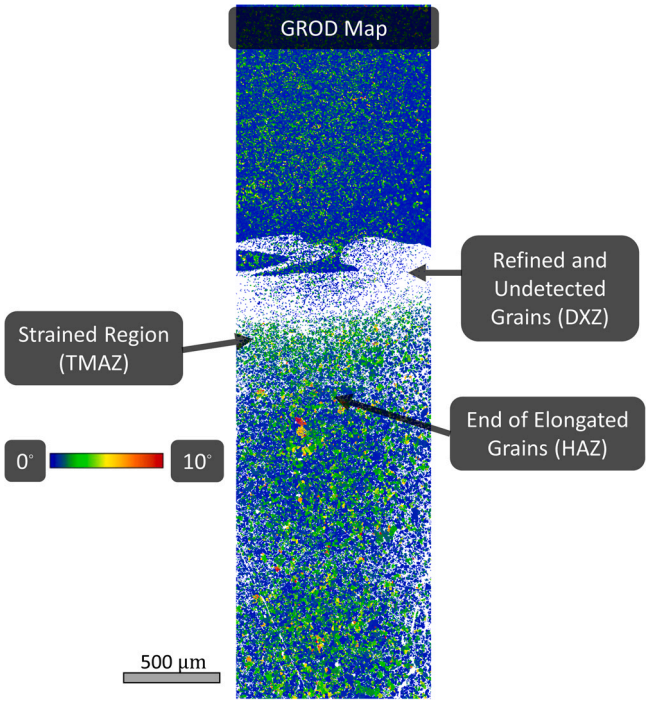

Fig. 18. The effects of the TMAZ on a GROD map at the center of the weld.

cases, the microstructural advancing side marker corresponds to the residual stress peak on the advancing side of the tool shown in Fig. 13.

Moreover, the resulting material flow creates the microstructure shown in Fig. 17, where the DXZ results in a reduced magnitude of grain sizes that are more refined compared to the thermo-mechanically affected zone (TMAZ), heat-affected zone (HAZ) and base-metal. Fundamentally the grain refinement depends on strain rate and thermal conditions, primarily determined by the tool rotation and traverse speed [27]. When the tool rotation decreases and the tool traverse speed increases, the heat input is reduced, and the average grain size decreases in the DXZ [38]. Therefore, the average grain size grows with increasing heat input from increasing the rotational speed and/or decreasing the traversal speed [9]. A finer microstructure is obtained with less heat, subsequently improving the material's mechanical properties. However, this strengthening mechanism is limited to a small processing window in FSW, as welding defects form if temperatures are too low. In contrast, if temperatures are too high and the materials start to melt, new phases may evolve, which could impact the strength of the friction-stir-welded joints. As mentioned above, welding temperatures are significantly determined by rotational speeds. Arbegast and Hartley [2] represent the peak temperature empirically in Eq. 4. Where T is the maximum temperature during welding (°C), T_m is the melting temperature of the material (°C), V is the tool traverse speed, ω is the rotational tool speed, and finally, α and K are material-dependent constants.

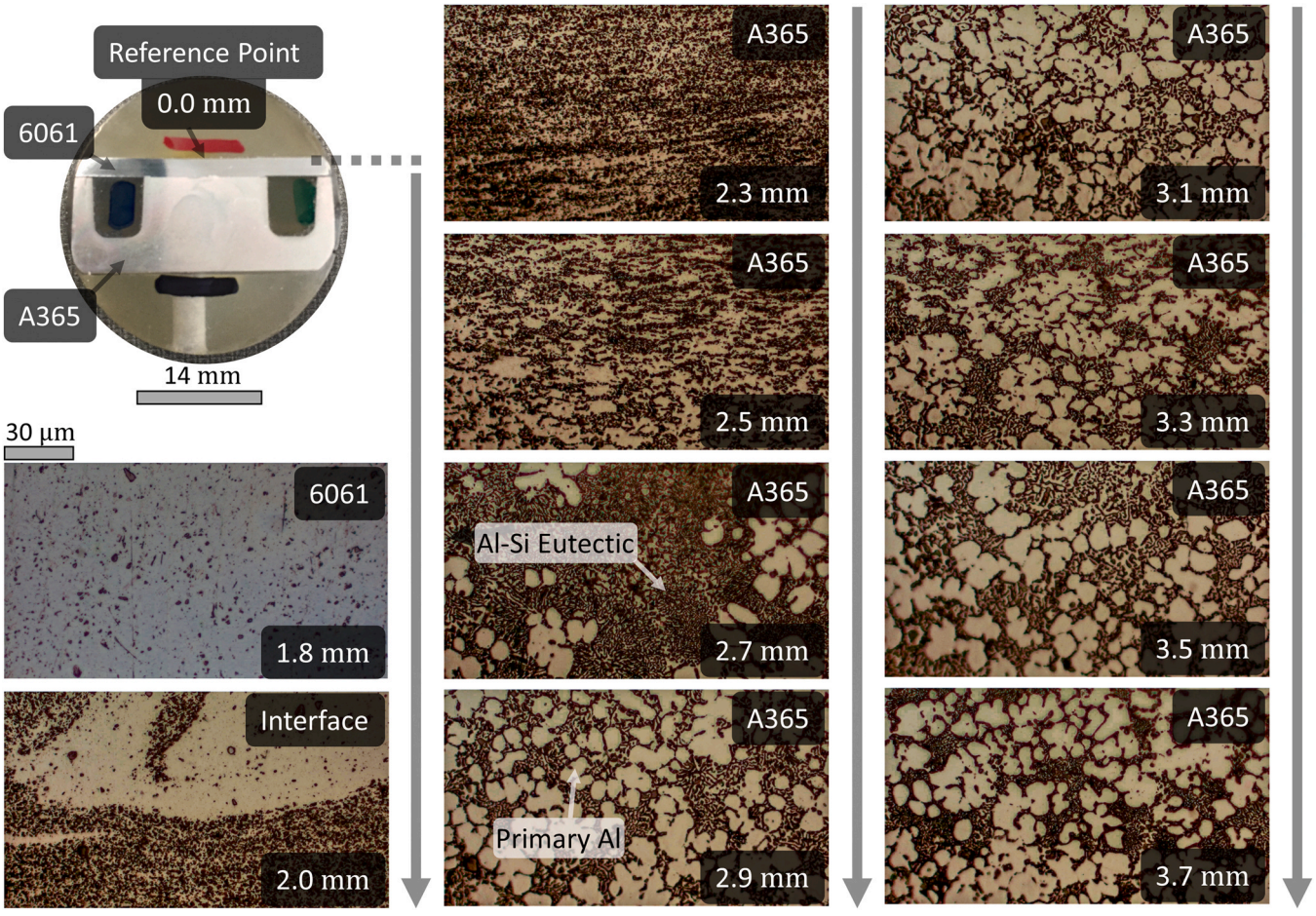

Fig. 19. Stepping optical microscope images (all micrographs taken at 100x magnification).

$$\frac{T}{T_m} = K\left[\frac{\omega^2}{V \cdot 10^4}\right]^{\alpha} \quad (4)$$

The ratio of ω^2/V, in Eq. 4, demonstrates that increasing the rotational speed with constant traverse speed or decreasing the traverse speed with constant rotational speed leads to higher welding temperatures. Additionally, the ratio of ω^2/V signifies the rotational speed's dominant effect on maximum welding temperature in the DXZ. Nevertheless, both rotational and traverse speeds need to be picked carefully to stay in the processing window for FSW.

Similarly, to the DXZ, in the TMAZ, the FSW tool plastically deforms the material and creates heat. However, aluminum can withstand significant plastic strain until recrystallization occurs. The plastic strain below this temperature results in a distinct boundary between the recrystallized DXZ and the deformed zones of the TMAZ [27]. One way to visualize the deformed TMAZ is with a Grain Relative Orientation Deviation (GROD) map shown in Fig. 18. The GROD map takes the average orientation of each grain and plots the deviation away from the average orientation for all other grains. Concerning the wrought plate, the average orientation represents a strong rolled-type texture, shown by the nearly solid blue in the 6061 (see Fig. 18). Below the joint in the cast A365, a random texture with no preferred orientation is shown by the many varying angles between 0° (blue) and 10° (red), characteristic of an as-cast random texture. However, just below the DXZ, in TMAZ, there is a definite texture created in the previously random as-cast material. As a result, the grains in the TMAZ do not recrystallize and instead become plastically strained and elongated. The same DXZ to TMAZ boundary is also observable in the 6061 material; however, the visual transition between the regions is harder to identify as the final grain size in the DXZ is heavily dependent on the initial size of the grain. The plate, 6061, is a wrought alloy that has undergone multiple processing steps that reduce its initial grain size before welding. While the cast A365 has no other processing to refine its initial grain size, thus making the A365 grain size orders of magnitude larger than the 6061 alloy. After welding, the A365 has undergone significant grain reduction because of its large initial grain size. The small 6061 grains, in comparison, reduce much less as they are recrystallized during welding. In some cases, the average grain size in the material with a very fine grain structure will increase after FSW.

Several optical microscope images are taken progressively into the material to confirm the end of the TMAZ and to view the possible formation of new phases at the weld interface, signifying possible melting during FSW. The first micrograph in Fig. 19 is the 6061 material, taken 1.8 mm away from the reference point (surface of the material), as shown in the macro image of Fig. 19. The next micrograph contains the 6061 and A365 cast interface, 2.0 mm away from the 0.0 mm reference. The small black and white phases are Al-Si eutectic, and the solid white grains are primary Al. The generated heat and "mixing" from the TMAZ recrystallize and deform the undistorted microstructure of the A365 until the 2.9 mm mark. After the 2.9 mm mark, the tool's interactions with the above material have no visible effect on the A365 microstructure, signifying the end of the TMAZ and the start of the HAZ.

The interface image at the 2.0 mm position in Fig. 19 shows no formation of phases between the A365 and 6061. This lack of interfaced phases is supported by isolating a dominant element in one of the materials. The silicon (Si) in the A365 (9.73 Si wt%.) material is in high concentration as compared to the 6061 (0.70 Si wt%.) material (see Table 1). The Si in the A365 is tracked utilizing SEM and Energy-dispersive X-ray Spectroscopy (EDS) by identifying the K-alpha emission lines unique to Si [12]. In Fig. 20, the high Si content is strictly contained in the A365 material. Even in the heavily recrystallized areas where the A365 grain size is most refined, the

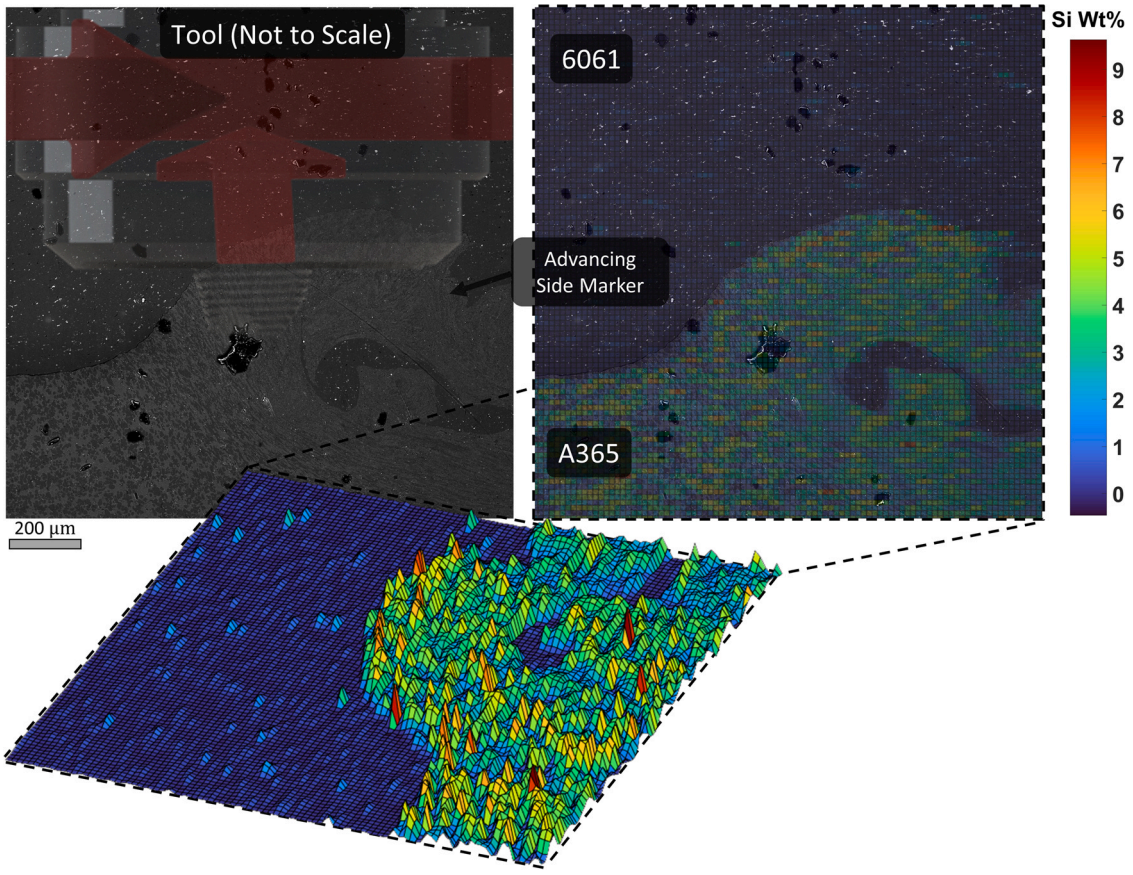

Fig. 20. A365-6061 silicon transition.

6061 and A365 materials do not mix into a material with a new chemical composition. This lack of mixing suggests that the plasticized pieces during the FSW operation strictly stir the material and do not mix, leading to a hard transition between 6061 and A365. This observation further reinforces that the operation conducted for this experiment was in a solid state, where the material did not transition into liquid form. While true for this study, this no-melting observation may not be valid for all FSWs, as process parameters can be adjusted to increase temperature and achieve melting in the DXZ.

Conclusions

Using the widely studied 6061 and A365 Al system, the effect of the welding conditions, including the material position, microstructure, and resulting residual stress in a wrought-to-cast lap FSW has been demonstrated and characterized using neutron diffraction, EBSD, and optical imaging techniques. Within the range of the welding conditions used, the conclusions are as follows:

(1) The EBSD analysis of a weldment portion reveals that in a sample area of the weldment, the orientation of grains depends on the FSW operation parameters, such as rotational and traverse directions, which produce varying elasticity across the weldment. Furthermore, the varied elasticity across the weldment creates a unique stress-free *d*-spacing profile corresponding to the tool rotation during welding.
(2) The tool's rotation and transverse direction, with respect to the geometric constraints of the component, influence the residual stress profiles. For example, if the rotational and traverse direction switched, the stress profile would mirror along the vertical axis, with the maximum tensile stress consistently occurring on the advancing side of the tool rotation direction.
(3) Unintentional preheating of the battery tray, by welds occurring in the proximity of un-welded locations, results in a decrease of maximum tensile stress after these un-welded locations become welded.
(4) Microstructural marks and residual stress results indicate that the advancing side of the tool rotation is consistent with the maximum residual stress location, where the advancing side's maximum stress can be 70% higher than the tool's retreating side.
(5) The EDS analysis of a weldment portion reveals the maximum silicon content through the 6061 to A365 FSW interface, suggesting that the plasticized pieces during the FSW operation strictly stir the material and do not mix, leading to a hard transition between 6061 and A365 from a lack of temperatures high enough for fusion.

Acknowledgments

This research was made possible in part due to the professional expertize and advice of Dr. Glenn Byczynski and Dr. Anthony Lombardi, as well as the financial support of Nemak Canada. Additionally, a portion of this research used the expertize of Dr. Andrew Payzant, Dr. Jeff Bunn, Paris Cornwell and resources at the High Flux Isotope Reactor at the DOE Office of Science User Facility operated by the Oak Ridge National Laboratory.

References

[1] Andrade, D.G., Leitao, C., Dialami, N., Chiumenti, M., Rodrigues, D.M., 2020, Modelling Torque and Temperature in Friction Stir Welding of Aluminium Alloys. International Journal of Mechanical Sciences, 182:1–11.
[2] Arbegast, W.J., Hartley, P.J., 1998, Friction Stir Weld Technology Development at Lockheed Martin Michoud Space System-an Overview. Trends in Welding Research, 4:541–546.
[3] Aval, H.J., 2015, Microstructure and Residual Stress Distributions in Friction Stir Welding of Dissimilar Aluminium Alloys. Materials & Design, 87:405–413.
[4] Bozkurt, Y., Salman, S., Çam, G., 2013, Effect of Welding Parameters on Lap Shear Tensile Properties of Dissimilar Friction Stir Spot Welded Aa 5754-H22/2024-T3 Joints. Science and Technology of Welding and Joining, 18:337–345.
[5] Çam, G., İpekoğlu, G., Tarık Serindağ, H., 2014, Effects of Use of Higher Strength Interlayer and External Cooling on Properties of Friction Stir Welded Aa6061-T6 Joints. Science and Technology of Welding and Joining, 19:715–720.
[6] Çam, G., Javaheri, V., Heidarzadeh, A., 2022, Advances in Fsw and Fssw of Dissimilar Al-Alloy Plates. Journal of Adhesion Science and Technology, 1:1–33.
[7] Campanelli, S.L., Casalino, G., Casavola, C., Moramarco, V., 2013, Analysis and Comparison of Friction Stir Welding and Laser Assisted Friction Stir Welding of Aluminum Alloy. Materials, 6:5923–5941.
[8] El-Sayed, M.M., Ahmed, S.Y., Abd-Rabou, M.M., Elsherbiny, M.G., 2021, Welding and Processing of Metallic Materials by Using Friction Stir Technique: A Review. Journal of Advanced Manufacturing and Processing, 3:1–20.
[9] Fadaeifard, F., Matori, K.A., Aziz, S.A., Zolkarnain, L., Rahim, M.A., 2016, Effect of the Welding Speed on the Macrostructure, Microstructure and Mechanical Properties of Aa6061-T6 Friction Stir Butt Welds. Metals, 7:1–16.
[10] Ganguly, S., Edwards, L., Fitzpatrick, M.E., 2011, Problems in Using a Comb Sample as a Stress-Free Reference for the Determination of Welding Residual Stress by Diffraction. Materials Science and Engineering A, 528:1226–1232.
[11] Giorgi, M.D., Scialpi, A., Panella, F.W., Filippis, L. a C.D., 2009, Effect of Shoulder Geometry on Residual Stress and Fatigue Properties of Aa6082 Fsw Joints. Journal of Mechanical Science and Technology, 23:26–35.
[12] Goldstein, J.I., Newbury, D.E., Echlin, P., Joy, D.C., Lyman, C.E., Lifshin, E., Sawyer, L., Michael, J.R., 2003, Scanning Electron Microscopy and X-Ray Microanalysis. third ed. Plenum, New York: 504–505.
[13] He, J., Li, H., Ling, Z., 2015, Effect of Tool Rotational Speed on Residual Stress, Microstructure, and Tensile Properties of Friction Stir Welded 6061-T6 Aluminum Alloy Thick Plate. International Journal of Advanced Manufacturing Technology, 84:1953–1961.
[14] Heidarzadeh, A., Mironov, S.Y., Kaibyshev, R., Çam, G., Simar, A., Gerlich, A.P., Khodabakhshi, F., Mostafaei, A., Field, D.P., Robson, J.D., Deschamps, A., Withers, P.J., 2021, Friction Stir Welding/Processing of Metals and Alloys: A Comprehensive Review on Microstructural Evolution. Progress in Materials Science, 117:1–68.
[15] Hidnert, P., Krider, H.S., 1952, Thermal Expansion of Aluminum and Some Aluminum Alloys. Journal of Research of the National Bureau of Standards, 48:209–220.
[16] Holden, T.M., Schajer, G.S., 2013, Practical Residual Strees Measurement Methods. Wiley, Virginia: 195–223.
[17] Hutchings, M.T., Withers, P.J., Holden, T.M., Lorentzen, T., 2005, Introduction to the Characterization of Residual Stress by Neutron Diffraction. CRC Press, Boca Raton: 1–21.
[18] İpekoğlu, G. & Çam, G. 2014. Effects of Initial Temper Condition and Postweld Heat Treatment on the Properties of Dissimilar Friction-Stir-Welded Joints between Aa7075 and Aa6061 Aluminum Alloys. METALL MATER TRANS A, 45, 3074–3087.
[19] İpekoğlu, G., Küçükömeroğlu, T., Aktarer, S.M., Sekban, D.M., Çam, G., 2019, Investigation of Microstructure and Mechanical Properties of Friction Stir Welded Dissimilar St37/St52 Joints. Materials Research Express, 6:1–8.
[20] James, M.R., 1987, Relaxation of Residual Stresses an Overview. Adv Surf Treat, 4:349–365.
[21] Kridli, G.T., Boileau, J.M. & Friedman, P.A. 2010. Manufacturing Processes for Lightweight Alloys. Woodhead, Cambridge, UK.
[22] Kumar, N., Mishra, R., Yuan, W., 2015, Friction Stir Welding of Dissimilar Alloys and Materials. CRC Press, New York: 7–8.
[23] Liu, L., 2010, Welding and Joining of Magnesium Alloys to Aluminum Alloys. Weld Join Technol, 63:38–62.
[24] Liu, T., Bunn, J.R., Francher, C.M., Nastac, L., Arvikar, V., Levin, L., Brewer, L.N., 2020, Neutron Diffraction Analysis of Residual Strain in High-Pressure Die Cast A383 Engine Blocks. J Mater Eng Perform, 29:5428–5434.
[25] Mccune, R.W., Murphy, A., Price, M., Butterfield, J., 2012, The Influence of Friction Stir Welding Process Idealization on Residual Stress and Distortion Predictions for Future Airframe Assembly Simulations. Journal of Manufacturing Science and Engineering, 134:1–9.
[26] Mehta, K.P., Patel, R., 2019, On Fsw Keyhole Removal to Improve Volume Defect Using Pin Less Tool. Key Engineering Materials, 821:215–221.
[27] Mishra, R.S., De, P.S., Kumar, N., 2014, Friction Stir Welding and Processing. Springer, Switzerland: 163–168.
[28] Mohammadi, J., Behnamian, Y., Mostafaei, A., Izadi, H., Saeid, T., Kokabi, A.H., Gerlich, A.P., 2015, Friction Stir Welding Joint of Dissimilar Materials between Az31b Magnesium and 6061 Aluminum Alloys: Microstructure Studies and Mechanical Characterizations. Materials Characterization, 101:189–207.
[29] Nile, L., Wu, Y.X., Gong, H., 2020, Prediction of Temperature and Residual Stress Distributions in Friction Stir Welding of Aluminum Alloy. International Journal of Advanced Manufacturing Technology, 106:3301–3310.
[30] Nishikawa, S., Kikuchi, S., 1928, The Diffraction of Cathode Rays by Calcite. in: Proceedings of the Japan Academy, 122:475–477.
[31] Noyan, I.C., Cohen, J.B., 1987, Residual Stress: Measurement by Diffraction and Interpretation. Springer-Verlag, New York: 15–27.
[32] Paradowska, A., Finlayson, T., Price, J.W.H., Ibrahim, R., Steuwer, A., Ripley, M., 2006, Investigation of Reference Samples for Residual Strain Measurements in a Welded Specimen by Neutron and Synchrotron X-Ray Diffraction. Physica B, 385:904–907.

[33] Pecharsky, V.K., Zavalij, P.Y., 2009, Fundamentals of Powder Diffraction and Structural Characterization of Materials. Springer,, US, Boston: 173–174.
[34] Peel, M.J., Steuwer, A., Michael, P., Withers, P.J., 2003, Microstructure, Mechanical Properties and Residual Stresses as a Function of Welding Speed in Aluminium Aa5083 Friction Stir Welds. Acta Materialia, 51:4791–4801.
[35] Richards, D.G., Prangnell, P.B., Williams, S.W., Withers, P.J., 2008, Global Mechanical Tensioning for the Management of Residual Stresses in Welds. Mater Sci Eng A, 489:351–362.
[36] Richards, D.G., Prangnell, P., Withers, P.J., Williams, S.W., 2013, Efficacy of Active Cooling for Controlling Residual Stresses in Friction Stir Welds. Science and Technology of Welding and Joining, 15:156–165.
[37] Sediako, D., D'elia, F., Lombardi, A., Machin, A., Ravindran, C.R., Hubbard, C., Mackay, R., 2011, Application of Neutron Diffraction in Analysis of Residual Stress Profiles in the Cylinder Web Region of an as-Cast V6 Ai Engine Block with Cast-in Fe Liners. SAE Int. J Mater Manuf, 4:299–308.
[38] Sedmak, A.S., Kumar, R., Chattopadhyaya, S., Hloch, S., Tadic, S.S., Djurdjevic, A.A., Cekovic, L.R., Donceva, E., 2016, Heat Input Effect of Friction Stir Welding on Aluminum Alloy Aa 6061-T6 Welded Joint. Therm Sci, 20:637–641.
[39] Soysal, T., Kou, S., Tat, D., Pasang, T., 2016, Macrosegregation in Dissimilar-Metal Fusion Welding. Acta Materialia, 110:149–160.
[40] Wang, L., Makhlouf, M., Apelian, D., 1995, Aluminium Die Casting Alloys: Alloy Composition, Microstructure, and Properties-Performance Relationships. International Materials Reviews, 40:221–238.
[41] Wang, M., Hu, H., 2013, Fusion Welding of Vacuum High Pressure Die Cast Aluminum Alloy A356 and Wrought Alloy 6061. SAE International Journal of Materials and Manufacturing, 6:299–303.
[42] Wayne, T.M., 1993, Friction - Friend or Foe? Metal Deposition by Friction and Resistance Techniques. Engineering Design, 5:4–8.
[43] Woodtli, J., Muster, W., Radon, J.C., 1986, Residual Stress Effects in Fatigue Crack Growth. Engineering Fracture Mechanics, 24:399–412.
[44] Zhao, J., Wu, C., Shi, L., 2022, Effect of Ultrasonic Field on Microstructure Evolution in Friction Stir Welding of Dissimilar Al/Mg Alloys. Journal of Materials Research and Technology, 17:1–21.